Accepted Manuscript

Full length article

Accelerated hardening of nanotextured 3D-plotted self-setting calcium phosphate inks

Santiago Raymond, Yassine Maazouz, Edgar B. Montufar, Roman A. Perez, Borja González, Joanna Konka, Jozef Kaiser, Maria-Pau Ginebra
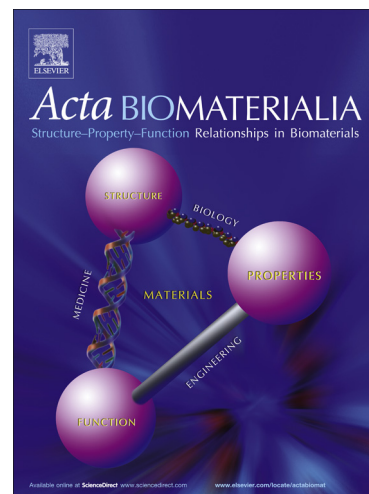
Please cite this article as: Raymond, S., Maazouz, Y., Montufar, E.B., Perez, R.A., González, B., Konka, J., Kaiser, J., Ginebra, M-P., Accelerated hardening of nanotextured 3D-plotted self-setting calcium phosphate inks, *Acta Biomaterialia* (2018), doi: https://doi.org/10.1016/j.actbio.2018.05.042

Accelerated hardening of nanotextured 3D-plotted self-setting calcium phosphate inks

Santiago Raymond[1,2,3‡]*, Yassine Maazouz*[1,2,3‡]*, Edgar B. Montufar*[1,4]*, Roman A. Perez*[1,5]*, Borja González*[1]*, Joanna Konka*[1,2]*, Jozef Kaiser*[4]*, Maria-Pau Ginebra*[1,2,6*]

[1] Dept. Materials Science and Metallurgical Engineering, Group of Biomaterials, Biomechanics and Tissue Engineering, Universitat Politècnica de Catalunya (UPC), Barcelona, Spain

[2] Barcelona Research Centre for Multiscale Science and Engineering, Universitat Politècnica de Catalunya (UPC), Barcelona, Spain

[3] Mimetis Biomaterials, Cerdanyola del Vallès, Barcelona, Spain

[4] CEITEC - Central European Institute of Technology, Brno University of Technology, Brno, Czech Republic.

[5] UIC Regenerative Medicine Research Institute. Universitat Internacional de Catalunya (UIC), Barcelona, Spain

[6] Institute for Bioengineering of Catalonia (IBEC), The Barcelona Institute of Science and Technology, Baldiri Reixac 10-12, 08028 Barcelona, Spain

‡These two authors have contributed equally to this work.

Abstract

Direct ink writing (DIW) techniques open up new possibilities for the fabrication of patient-specific bone grafts. Self-setting calcium phosphate inks, which harden at low temperature, allow obtaining nanostructured scaffolds with biomimetic properties and enhanced bioactivity. However, the slow hardening kinetics hampers the translation to the clinics. We explored different hydrothermal treatments for the consolidation of DIW scaffolds fabricated with an α-tricalcium phosphate /pluronic F127 ink, comparing them with a biomimetic treatment. Three different scaffold architectures were analysed. The hardening process, associated to the conversion of α-tricalcium phosphate to hydroxyapatite was drastically

1

accelerated by the hydrothermal treatments, reducing the time for complete reaction from 7 days to 30 minutes, while preserving the scaffold architectural integrity and retaining the nanostructured features. β-tricalcium phosphate was formed as a secondary phase, and a change of morphology from plate-like to needle-like crystals in the hydroxyapatite phase was observed. The binder was largely released during the treatment. The hydrothermal treatment resulted in a 30% reduction of the compressive strength, associated to the residual presence of β-tricalcium phosphate. Biomimetic and hydrothermally treated scaffolds supported the adhesion and proliferation of rat mesenchymal stem cells, indicating a good suitability for bone tissue engineering applications.

1 Introduction

The recent developments in three dimensional (3D) printing technologies have opened vast opportunities for the development of patient-specific bone grafts, which is expected to have a particularly high impact on dental and maxillofacial surgery as well as in trauma and orthopaedic surgery. Whereas autologous or allogenic bone grafts are still the gold standard in the frequent bone grafting surgical procedures performed nowadays,[1,2] the possibility to fabricate customised scaffolds based on digitalised medical imaging techniques has provided a real boost to the applications of synthetic bone grafts. The novel fabrication approaches referred to as 3D printing techniques are based on computer aided design (CAD) and computer aided manufacturing (CAM) and result in a patient-specific bone grafting therapy. Such technologies allow the design of personalised synthetic bone grafts, matching the specificity of every defect in terms of both the metabolic and anatomic characteristics, opening new perspectives in this field.[3]

Previous works reported the use of such techniques employing polymers, ceramics, or even metal alloys.[4,5] In the case of bioceramics, the works revolve around either powder bed printing, which consists

2

in dispensing a liquid binder or reactive fluid onto a powder bed in a layer by layer process,[6] or in filament-based direct ink writing (DIW), also referred to as robocasting, microextrusion or three-dimensional plotting [7] which consists in dispensing layer by layer an ink composed of ceramic particles homogenously dispersed in a binder following an *in silico* designed pattern. The main advantage of filament-based direct ink writing over powder bed printing is that there is no need to clean the printed object from remaining particles from the bed that can provoke adverse inflammatory responses of the host tissue. The design of the inks plays a central part in this technology. They must present a pseudoplastic behaviour in order to withstand the weight of the superimposed layers and must be completely injectable, allowing a continuous printing.[8] Furthermore, by tailoring the ink composition it is possible to tune the physicochemical properties of the scaffolds in terms of chemistry, textural properties and multiscale porosity.

The use of DIW with calcium phosphate (CaP)-based inks for the fabrication of bone implants and scaffolds for bone tissue engineering was proposed for the first time in 2005.[9] Several works have reported the fabrication and properties of robocasted scaffolds made of hydroxyapatite (HA),[9–11] beta tricalcium phosphate (β-TCP) [12,13], biphasic combinations of β-TCP and HA [11,14–17] and bioactive glasses.[18–24]

Nonetheless, in all these pioneer works, after DIW the samples had to be consolidated by sintering at high temperature. The effects of sintering conditions on the chemical, structural and mechanical properties of those samples have been deeply studied.[11,16,25,26]

Recently, the possibility to fabricate low-temperature self-setting inks that do not require the sintering step has been proposed, using formulations based on beta-calcium silicate (β-CaSiO$_3$),[20,27] magnesium phosphates[28] or calcium phosphates.[29,30] Most calcium phosphate self-setting inks are based on alpha-tricalcium phosphate (α-TCP), which can be combined with different binders, like gelatine,[29] type I collagen[31] hydroxypropyl methylcellulose (HPMC),[32] Polysorbate 80 (Tween 80) and short-chain triglycerides (Miglyol 812),[30,33,34] polyvinyl alcohol[33] and alginic acid.[33] The hardening process of

3

these inks is due to the hydrolysis of α-TCP to a calcium deficient hydroxyapatite (CDHA), resulting in nano/micro structured crystals that are much closer to the mineral phase of bone than sintered CaPs. In this work, we propose to exploit the inverse-thermoresponsive properties of pluronic F127, using it as a new binder for an α-TCP self-setting ink. We showed in a previous work that the combination of pluronic F127 hydrogel with alpha-TCP resulted in a paste exhibiting a sequential gelling/hardening behaviour and enhanced injectability. Moreover, the presence of pluronic did not hinder the self-hardening reaction of alpha-TCP.[35]

However, while the low-temperature chemical consolidation of these scaffolds allows obtaining a biomimetic product, closer to bone mineral than the high-temperature sintered scaffolds, the self-setting reaction of the α-TCP-based inks is slow, and therefore the hardening process of the 3D-printed scaffolds is long. This makes the translation of this technology to the clinic complex, and impairs its application, particularly in emergencies where time is valuable and limited. It is therefore necessary to accelerate the hardening process. With this objective in mind, in this work we analyse different post-printing treatments for DIW scaffolds fabricated with a pluronic F127/α-TCP self-setting ink, and their effect on the nano/microstructure, composition and mechanical performance, as well as on the ability to sustain the proliferation of mesenchymal stromal cells.

2   Materials and Methods

2.1   Preparation of the self-setting Ink

The solid phase of the self-setting ink was composed of α-TCP synthesised as described elsewhere.[36] The α-TCP block was milled in an agate planetary ball mill (Fritsch, Pulverisette) during 15 min at 450 rpm with 10 agate balls (30 mm diameter). The resulting powder was then sieved during 30 min with a 40 µm sieve (Filtra, Spain), introducing 145 g of powder together with 200 g of Zirconia balls (1.5 mm diameter; Tosoh, Japan). The binder phase of the ink was prepared introducing 30 g of pluronic F127 (Sigma Aldrich P2443) together with 50 mL of distilled water in a 150 mL polypropylene (PP) recipient (Dürmann, Germany) and

4

mixed in a dual asymmetric centrifugal mixer (DAC 150, Speedmixer, USA) at 3500 rpm during 1 min. Water was then added to a total volume of 100 mL and the mixture was homogenised in the DAC mixer at 3500 rpm for 5 min. The ceramic ink was finally produced by introducing 6 g of α-TCP powder together with 3 g of binder solution (binder to powder ratio of 0.5 g g^{-1}) into a PP recipient of 50 mL and mixed for 1 min at 3500 rpm in the DAC mixer.

2.2   Computer Aided Design and DIW Process

Cylindrical samples (6 mm diameter and 12 mm height) were designed with the help of a CAD software (Solidworks, Dassault Systems, France) and exported into a stereo lithography (STL) file. The resulting STL file was then transferred to the open source software Slic3r (slic3r.org) in order to adjust the fabrication parameters. As described in Figure 1**,** three patterns with different architectures were fabricated. The orthogonal pattern (O) corresponded to a 90° rotation at each layer of a linear parallel grid. The orthogonal rotated (OR) pattern corresponded to a 45° rotation at each layer of the linear parallel grid. The honeycomb (HC) pattern was composed of hemi-hexagonal segments which were rotated 120° at each layer, composing hexagons when the structure was projected onto the XY plane. In all cases the nozzle size (theoretical strand diameter) was set to 250 μm, the layer height to 225 μm (corresponding to a layer overlapping of 10 % along the Z axis), the filling density was set to 45 % and the deposition speed was set to 10 mm s^{-1}. This information was saved in a numerical control programming language (G-code).

Prior to printing the scaffolds, the self-setting ink was introduced into the cartridge (3cc Optimum® Syringe Barrels, Nordson EFD, U.S.A.). Then, a tapered dispending tip (Gauge 25 SmoothFlow Tapered Tips, Nordson EFD, U.S.A.) was coupled to the cartridge, and the whole assembly was installed into the DIW device (Pastecaster, Fundació CIM, Spain). Afterwards, batches of 15 scaffolds were fabricated at room temperature in a time span of 1.5 h.

2.3   Post-printing Hardening Treatments

5

The fabricated scaffolds were then subjected to three different post-printing processes, as described in Figure 2: (a) biomimetic treatment, where the scaffolds were immersed in water at 37°C for up to 6 days, using a fixed volume of 100 mL per scaffold. Prior to immersion, the scaffolds were kept in a water vapour saturated atmosphere at 37°C for 24 h to ensure good cohesion; (b) hydrothermal-immersed treatment, where the specimens were immersed in water (100 mL per scaffold) and autoclaved at 121°C and 2 atm of absolute pressure for different time lengths, up to 30 minutes; (c) hydrothermal-vapour treatment, where the scaffolds were autoclaved at 121°C and 2 atm of absolute pressure for different time lengths, up to 100 minutes. Prior to both hydrothermal treatments, the specimens were kept in a vapour saturated atmosphere at 100°C and 1 atm for 10 minutes.

Scaffold Characterisation – Phase Composition and Microstructure: Phase composition was assessed at different reaction times by X-ray powder diffraction on the powder obtained for each hardening condition after manually crushing the scaffolds in an agate mortar. In the case of scaffolds subjected to the biomimetic treatment, samples were immersed in isopropanol during 15 min prior to the analysis to stop the hardening reaction at selected times. The diffractometer (D8 Advance, Bruker) equipped with a Cu Kα X-ray tube was operated at 40 kV and 40 mA. Data were collected in 0.02° steps over the 2θ range of 10–80° with a counting time of 2 s per step. Phase quantification was performed using the reference intensity ratio method (EVA, Bruker) comparing diffraction patterns of the crystalline structures of α-TCP (ICDD PDF 00-029-0359), CDHA (ICDD PDF 01-086-1201) and β-TCP (ICDD PDF 00-003-0681).

The microstructure of the scaffolds hardened in different conditions was observed under a field emission scanning electron microscope (FIB/SEM, Zeiss Neon 40) at 5 kV, after coating the surface with a thin carbon layer.

2.4 Scaffold Characterisation – Scaffold Architecture, Porosity and Specific Surface Area

X-ray computed microtomography (μCT) analysis was conducted using the GE phoenix v|tome|x L 240 system equipped with a 180 kV/20 W maximum power nanofocus X-ray tube and high contrast flat panel detector DXR250. The tomographic measurement was performed with an acceleration voltage of 80 kV and

an X-ray current of 150 µA. The X-ray spectrum of tungsten target was modified by using a 0.5 mm thick aluminium filter. The exposure time per projection was 400 ms and 1800 projections were taken around 360°. The isotropic linear voxel size (voxel resolution) of the obtained volume was 15 µm. The sample tomographic reconstruction was performed with GE phoenix datos|x 2.0 software, using the object shifting correction and the beam hardening correction in the different material modes. The visualization of the samples, as well as the structural parameter quantifications, were performed using VG Studio MAX 2.2 software. Three scaffolds were scanned at the same time allowing the use of the same threshold values for segmentation. Surface determination tool within VG Studio was used to display the sample volume in virtual reconstructions.

In addition, open porosity and pore entrance size distribution were analysed in the range between 0.006 and 360 µm by mercury intrusion porosimetry (MIP, AutoPore IV Micromeritics). The volume of nano-micropores normalised per unit of mass (V_{micro}) was measured from the sum of the incremental mercury intrusion in the pores smaller than 10 µm.

The skeletal density of the scaffolds (ρ_{skel}) was assessed by helium pycnometry (AccuPyc 1330, Micromeritics, USA).

The apparent density of the scaffolds (ρ_{app}) was calculated as the quotient of the scaffold mass over the scaffold equivalent cylinder volume obtained from the measurements of the scaffold diameter and height.

The value of the total porosity (P_{TOT}) was calculated with the Eq.1:[37]

$$P_{TOT}(\%) = \left(1 - \frac{\rho_{app}\left[\frac{g}{cm^3}\right]}{\rho_{skel}\left[\frac{g}{cm^3}\right]}\right) \cdot 100 \tag{1}$$

The nano-microporosity (P_{micro}) was calculated with the Eq. 2:

$$P_{micro}(\%) = \left(V_{micro}\left[\frac{cm^3}{g}\right] \cdot \rho_{app}\left[\frac{g}{cm^3}\right]\right) \cdot 100 \tag{2}$$

The macroporosity (P_{macro}) was calculated as the difference between the total porosity and the nano-micro porosity (Eq.3)

$$P_{macro}(\%) = P_{TOT}(\%) - P_{micro}(\%) \tag{3}$$

Finally, the specific surface area (SSA) was determined by nitrogen adsorption using the BET (Brunauer-Emmett-Teller) method (ASAP 2020, Micromeritics). Prior to measurement, samples were outgassed in vacuum conditions (10 mmHg) at a holding temperature of 100 °C for 2 h.

2.5   Scaffold Characterisation – Binder Content Thermogravimetric Analysis and FTIR

 Thermogravimetric analysis (TGA) was performed with the aim to determine the amount of binder remaining in the scaffolds after the different consolidation methods. The measurements were performed under the heating rate of 10˚C min^{-1} from 25 to 550˚C in an oxygen saturated atmosphere. The amount of polymer contained in the scaffolds was determined by comparing the TGA curves of each sample with those of a pluronic-free counterpart, consisting of α-TCP mixed with water with the same L/P ratio and subjected to the same treatment as the corresponding sample.

Fourier-transform infrared (FTIR) spectroscopy analysis was performed in a Nicolet 6700 FTIR spectrometer using the KBr pellet method using 2 mg sample/ 300 mg KBr. Spectra were recorded in the 4000 to 400 cm^{-1} range, at 128 scans accumulation and 2 cm^{-1} resolution.

Scaffold Characterisation – Mechanical Characterization: A universal testing machine (Bionix, MTS) was employed to perform uniaxial compressive tests at a rate of 1 mm min^{-1}. The load was applied perpendicular to the printing plane (XY plane), *i.e.* in the Z direction. HC patterned scaffolds subjected to different post-printing treatments were tested, as well as scaffolds fabricated with different pattern architectures and hardened under biomimetic conditions. Samples were tested in wet state in order to be closer to the *in vivo* situation. A total of 12 scaffolds were tested for each condition. The Weibull modulus was calculated applying a Weibull statistical analysis on the ultimate compressive stress values (Eq. 4).

$$Ln\left(Ln\left(\frac{1}{P_s}\right) \right) = m(Ln(\sigma) - Ln(\sigma_0)) \tag{4}$$

Where:

P_s = Probability of survival

σ = ultimate compressive strength of the sample

σ_0 = constant corresponding to the stress for which 100 % of the samples will not fail

m = Weibull modulus

2.6 Scaffold Characterisation – Cell Culture

The influence of the post-printing treatment on cell response was studied in static 3D culture conditions in samples fabricated with O architecture. Scaffolds (discs of 6 mm in diameter and 2 mm in height) were placed in 24-well cell culture plates, sterilised with ethanol (70 %, Sigma and Aldrich) during 30 min and rinsed 3 times with phosphate buffer saline (PBS, Gibco). Samples were then preconditioned for 2 hours with 1 ml of advanced Dulbecco's Modified Eagle Medium supplemented with 10% fetal bovine serum, 2 mM L-glutamine, 50 U mL^{-1} penicillin, 50 μg mL^{-1} streptomycin and 20 mM HEPES. Afterwards, the medium was removed and $5x10^5$ rat mesenchymal stromal cells (rMSC; extracted from bone marrow of long bones of Lewis rats; in passages 3 to 5) were seeded on each scaffold in a 25 μl medium drop. rMSC were allowed to attach during 1 h at 37 °C and 5 % CO_2 and then 1 ml of fresh medium was gently added. After 3 and 7 days of static cell culture, the scaffolds were moved to a new well plate, rinsed with PBS and the remaining cells on the scaffolds were lysed with 500 μl of M-PER (mammalian protein extraction reagent, Thermo Scientific, Waltham, MA, USA). The cell number was quantified using a commercial lactate dehydrogenase (LDH) detection kit (Roche Applied Science, Penzberg, Germany). The LDH activity in the lysates was measured spectrophotometrically at a wavelength of 492 nm with PowerWave HT Microplate Reader (BioTek Instruments, Inc., Winooski, VT). A calibration curve with decreasing number of cells was used to express the results of LDH activity in cell number. Experiments were performed in triplicates for statistical analysis.

Immunofluorescent staining was used to visualise cell morphology. After 7 days of culture the scaffolds were rinsed in PBS–glycine and cells were fixed for 20 min in 4 % paraformaldehyde solution. Cells were

9

permeabilised for 15 min with Triton X-100 (0.05 %) and blocked for 30 min in PBS–bovine serum albumin (BSA; 1 %). Actin filaments were stained with TRITC-conjugated phalloidin (Sigma-Aldrich, USA) and nuclei were counterstained with DAPI (4',6-diamidino-2-phenylindole, 1 μg/ml). Images were acquired with an E600 fluorescence microscope (Nikon, Japan) and treated with Cell F software (Olympus, Japan).

2.7   Statistical analysis

Data were analysed using one-way analysis of variance and Tukey's multiple-comparison test to determine statistical differences between specimens. A confidence interval of 95% ($\alpha=0.05$) was used and the resulting means and standard deviations are shown in Figures 8 and 11.

3   Results and Discussion

3.1   Effect of the Post-printing Treatment on Composition, Microstructure and Porosity

The hardening of the scaffolds is associated to the hydrolysis of the α-TCP contained in the ink, which transforms to a calcium deficient hydroxyapatite (CDHA) according to the following reaction (Eq. 5):

$$3\alpha\text{-}Ca_3(PO_4)_2 \text{ (s)} + H_2O \text{ (l)} \rightarrow Ca_9(HPO_4)(PO_4)_5OH \text{ (s)} \tag{5}$$

The reaction mechanism involves the dissolution of the α-TCP particles followed by the nucleation and growth of CDHA crystals. This mechanism has been extensively studied in the field of calcium phosphate cements for the development of injectable bone grafting materials. [38,39] Moreover, in a previous work we demonstrated that the addition or pluronic F127 in α-TCP pastes slightly delayed the setting reaction in the early stages but did not hinder the full transformation to calcium-deficient hydroxyapatite [35]. The results obtained with the robocast scaffolds confirm these results since, as shown in Figure 3(a), under biomimetic conditions α-TCP fully transformed to CDHA in 3 to 7 days.

The hydrolysis of α-TCP under hydrothermal-immersed conditions (Figure 3(b)) displayed similarities with respect to the biomimetic conditions. However, the time required to yield the maximum conversion into

10

CDHA decreased to 15 minutes. The faster reaction kinetics is in agreement with previous studies which report that hydrolysis of α-TCP occurs more rapidly at increased temperatures,[40,41] and must be interpreted taking into account the retrograde solubility of both α-TCP and hydroxyapatite.[42,43] Thus, although the solubility of α-TCP is smaller at the higher temperature of the hydrothermal treatment, also the solubility of CDHA is reduced, thus fostering the precipitation of this compound and resulting in a higher reaction rate. Furthermore, β-TCP appeared as a result of the treatment, indicating that while α-TCP reacted to form CDHA, α-TCP also underwent allotropic phase transformation to form its low-temperature beta polymorph. As a result, the yield in CDHA formation was reduced to around 90 %.

The final composition of the scaffolds after the hydrothermal-vapour condition was significantly different from the other two treatments (Figure 3(c)). In this case, the final composition of the scaffold consisted in a mixture of CDHA (60 %), β-TCP (17 %) and unreacted α-TCP (23 %). The reaction time was around 60 min.

The formation of β-TCP as a second phase in addition to CDHA after the hydrothermal treatment of α-TCP was reported in previous studies,[44] although longer treatment times were applied. The formation of β-TCP was surprising since this phase is generally obtained by solid state reaction above 700 °C. The results obtained suggest that the pressure applied lowers the transition temperature between the β and α-TCP, which is close to 1120 °C, thus favouring the allotropic transformation of α-TCP into β-TCP. This transformation coexists with the hydrolysis of α-TCP to CDHA.

The post-printing treatment affected not only the phase transformation taking place in the scaffolds, but also the presence of binder after its consolidation. The nominal amount of binder added in the ink was calculated to be 14.3 wt%. The binder remaining in the scaffolds after the different post-printing treatments, once the phase transformation was complete (7 days, 30 min and 100 min for the biomimetic, hydrothermal-immersed and hydrothermal-vapour respectively), was measured by TGA (Figure 4(a)). The decomposition temperature of pluronic F127 was 200°C. Interestingly, a significant weight loss was observed in the control samples, that is, the samples prepared without pluronic. This can be attributed to the loss of water associated to the CDHA phase, both the evaporation of surface-adsorbed water, below

11

200°C, and further loss of the lattice water at higher temperatures.[45,46] The fact that this was more pronounced for the biomimetic sample than for the ones subjected to hydrothermal treatments can be associated to the higher amount of CDHA present in the specimens on one hand, and on the other hand to a higher water content in the former specimens. In fact, the shape of the curves suggests that specimens obtained by the biomimetic treatment had a higher amount of adsorbed water, which is associated to the weight loss below 200° C, whereas the amount of lattice water seemed to be similar to the samples subjected to the hydrothermal treatment, as reflected by the similar slopes of the curves above 200° C. Concerning the DIW scaffolds, the highest weight loss was observed for the hydrothermal vapour treatment, whereas the other two treatments, that is biomimetic and hydrothermal immersed, showed similar decomposition patterns of the binder, with lower weight loss observed. In Figure 4(b) the calculated values of the binder's amount in the different samples is displayed. As expected, in the hydrothermal vapour condition the content of pluronic F127 the treated specimens was the same as for the initial ink used (14.3%). In contrast, the amount of binder in the samples treated under biomimetic and hydrothermal immersed conditions was reduced to 0.36 and 0.53 %, demonstrating that during the immersion in water, either at 37 or 121°C, the binder contained in the scaffolds was almost completely released.

The FTIR spectra of the different specimens are displayed in Figure 5. The typical bands characteristic of the different PO_4 vibration modes of (v1~980, v2~363, v3~1082 and v4~515 cm^{-1}) [47] present in calcium phosphates were identified in all samples. Moreover, all samples, regardless of the hardening treatment used, presented the absorption bands of HPO^{2-}_4 (~870 cm^{-1}) and OH$^-$(~631 and ~3570 cm^{-1}) which are characteristic of calcium deficient hydroxyapatite [48] [49]. Although α-TCP and β-TCP were observed in the XRD patterns, these two phases were hardly distinguished in the FTIR spectra due to the overlapping of their infrared spectral bands with those of CDHA.

In addition, in the samples subjected to the hydrothermal-vapour process, C-H stretching bands (~2850 cm^{-1}) corresponding to sp3 carbon hydrogen bonds and C-O stretching bands (~1110 cm^{-1}) corresponding to alkoxy bond characteristic of aliphatic ethers, confirming the presence of pluronic F127 in the scaffolds [50], in agreement with the TGA results (Figure 4).

12

The microstructure of the scaffold strands after complete reaction for the different treatments (7 days, 30 min and 100 min for the biomimetic, hydrothermal-immersed and hydrothermal-vapour respectively) is shown in Figure 6. The biomimetic treatment resulted in an entangled network of plate-like CDHA crystals (Figure 6(a)), which is in agreement with the microstructure developed under biomimetic conditions in calcium phosphate cements prepared with coarse particles, similar to the ones used in the self-setting ink.[51] In contrast, in the hydrothermal-immersed condition the CDHA crystals exhibited a needle-like morphology (Figure 6(b)), as also reported in previous studies.[52] Under hydrothermal-vapour condition, the microstructure of the scaffold was consistent with a lower rate of transformation to CDHA, the original α-TCP particles being still visible, although covered with a layer of CDHA nanometric crystals (Figure 6(c)) that, according to XRD, represented 60 % of the composition of the scaffold. The lack of liquid environment hindered ionic diffusion and therefore the precipitated crystals were localised in close contact with the reactant particles. Although water vapour could be condensed on the surface of the particles, the ions produced by the dissolution of the α-TCP could not migrate to form an entangled network of CDHA crystals. Instead, the precipitated CDHA formed a compact shell that impaired the dissolution of the remaining α-TCP core.

The SSA values were 12.345 ± 0.004, 11.664 ± 0.033 and 2.342 ± 0.018 m^2 g^{-1} for the biomimetic, hydrothermally-immersed and hydrothermal-vapour samples, respectively, which are in good agreement with the microstructural observations.

The pore entrance size distribution of the scaffolds consolidated under the different methods determined by MIP is presented in Figure 7. In general, a bimodal pore entrance size distribution can be observed for each consolidation method. The pores larger than 10 μm corresponded to the macroporosity between strands. All the scaffolds used for the MIP were printed following the HC pattern, which made the entrance macropore size distribution overlap in all cases. In contrast, the entrance pore size distribution below 10 μm (nano-microporosity within the strands) presented significant differences between consolidation methods, due to the different microstructures obtained. The smallest micropores were observed for the scaffolds consolidated with the biomimetic approach, with pore entrance sizes bellow 0.1 μm. The

13

hydrothermal-immersed samples presented slightly bigger pore entrance sizes (around 0.2 μm). This is consistent with previous results obtained with calcium phosphate cements with similar composition, where it was shown that plate-like CDHA crystal networks resulted in smaller-size pore interconnections than the needle-like crystal networks.[37] Finally, the biggest pore entrance size (2 to 3 μm) was observed for the hydrothermal-vapour treatment. As it can be observed in Figure 6, the spaces between polyhedral particles in this sample are considerably larger than the spaces between plate- or needle-like crystals of the other samples.

The quantification of the nano-microporosity measured by MIP, as well as the total porosity calculated according to Eq. (1) and the macroporosity according to Eq. (3) is displayed in Figure 8(a). Remarkable differences were found in nano-micro porosity with values of 23.9, 26.7 and 15.3% for the biomimetic, hydrothermal-immersed and hydrothermal-vapour respectively. These differences explain the values found in the total porosity, which follow the same trend. The macroporosity was very similar for the three post-printing treatments (44.8, 45.9 and 44.0% for the biomimetic, hydrothermal-immersed and hydrothermal-vapour respectively) as expected since all the specimens were printed with the HC pattern.

3.2   Effect of the Post-printing Treatment on the Mechanical Properties

Figure 8(b) shows the compressive strength and Weibull modulus of scaffolds with HC pattern, after the different post-printing treatments. The hydrothermal treatments led to lower compressive strength and Weibull modulus compared to the biomimetic condition, with the hydrothermal-vapour presenting the lowest values. No correlation was observed between porosity and compressive strength, which suggests that the differences in microstructure plays a determinant role. In fact, previous studies on calcium phosphate cements revealed that the mechanism responsible for the hardening of these materials was the mechanical interlocking between the precipitated crystals, and that the mechanical strength was directly related to the amount of precipitated phase formed in the setting reaction.[38,53] This trend is clearly maintained in the present study, where the scaffolds under the hydrothermal-vapour treatment presented the lowest conversion into CDHA and the microstructure lacked entangled CDHA crystals. In contrast, the hydrothermal-immersed and the biomimetic scaffolds presented an increasing conversion into CDHA which

14

resulted in higher compressive strengths, which are within the range of the compressive strength of cancellous bone (between 2 and 12 MPa).[54]] An additional parameter that may contribute to the lower compressive strength of the hydrothermal-vapour samples is the plasticising effect of the binder, which was retained in much higher amounts (14.55%) than in the other treatments (Figure 4b). Moreover, the Weibull modulus of the biomimetic scaffolds was bigger than that of the hydrothermal-immersed scaffolds, which indicates that this last treatment results in less reliable samples (*i.e.* with a higher variability in the compressive strength). Since the mechanical reliability of brittle materials such as the CDHA scaffolds depends on the distribution of defects, it can be hypothesised that the presence of some β-TCP in the material can result in a more heterogeneous structure, this creating stress concentration sites. It would be important, therefore, to find strategies to enhance the reliability and toughness of this kind of structures.

3.3 Effect of Scaffold Pattern on Mechanical Properties

Scaffolds with different structures subjected to the biomimetic post-treatment were compared in terms of mechanical properties. Representative μCT reconstructions of the scaffolds fabricated following different patterns are shown in Figure 9, where a representative unit cell for each pattern obtained by μCT analysis is also displayed. For the O pattern, the macropore size, measured as the distance between adjacent parallel strand surfaces was $L_x = L_y = 332 \pm 18$ μm in the printing plane projection (XY plane), and $L_z = 195 \pm 15$ μm in the lateral projection. These distances were the same in the OR scaffolds, but the 45° rotation applied every layer created a more complex pore shape. The HC scaffold presented vertical hexagonal channels with average diameter of 556 ± 46 μm.

As expected, the different patterns resulted in different macroporosities, as shown in Figure 8(c). The HC pattern exhibited the lowest macroporosity (43.8 %), followed by the O pattern (53.5 %) and, finally, the OR (55.4%). Regarding the nano-micro porosity, the three conditions presented similar values (19.9, 19.2 and 23.0 % for O, OR and HC respectively), as all the samples were subjected to the same biomimetic setting treatment.

15

The compressive strength and Weibull modulus for the scaffolds with different patterns, all of them subjected to the biomimetic treatment are shown in Figure 8(d).The highest compressive strength and Weibull modulus corresponded to the HC scaffold, followed by the O and OR scaffolds.

No correlation was found between compressive strength and macroporosity. The trends observed can be rather explained by the strand architecture in the different scaffolds. Thus, in the HC pattern the strands form tubular-like walls aligned in the direction of the applied load, and in the case of the O patterned scaffold, the intersection points of the strands in the different layers also form longitudinal pillars (Figure 10). As previously described,[11,29,55] the failure of the structure is due to the bending of these pillars. The higher Weibull modulus of the HC pattern indicates that this structure is mechanically more reliable than the O pattern in the direction perpendicular to the printing plane. In the OR structure, the overlapping points between strands are shifted every two layers, which results in a drastic reduction of vertical pillars, leading to a significantly lower compressive strength. The percentage of area within the XY projection where the strands are overlapped in consecutive layers of a repetition unit (Figure 10), that is, the effective section, was 22% of the cross-section area for the O pattern, only 11% for the OR and 28% for the HC pattern, which is in good agreement with the trends observed for the compressive strengths measured for the different structures (Figure 8(d)).

It is difficult to compare the mechanical properties of the biomimetic scaffolds with analogous ceramic scaffolds fabricated by DIW, due to different porosities and architectures. Although in general higher compressive strengths were reported for sintered scaffolds, for example 47 and 15 MPa, for hydroxyapatite and beta tricalcium phosphate with O structure respectively,[11,16] it has to be considered that pore size and strut diameter were different from the ones in the present study, and especially, the total porosity was much smaller, around 40 %, whereas the biomimetic O scaffolds exhibited 73 % of total porosity.

3.4   *In Vitro* Response of Rat Mesenchymal Stromal Cells.

In order to assess the effect of the post-printing treatments on the ability of the scaffolds to support cell adhesion and growth, rMSC were seeded on O scaffolds subjected to the different conditions. As shown in

Figure 11, scaffolds hardened under biomimetic conditions supported cell adhesion, with a stable number of cells over time, while the number of cells slightly increased in the case of the scaffolds subjected to the hydrothermal-immersed treatment. In contrast, the number of cells on the hydrothermal-vapour treated scaffolds was significantly lower and decreased over time. Confocal microscopy images after 7 days of culture confirmed the presence of cells covering all the surface of the strands on the biomimetic and hydrothermal-immersed scaffolds, whereas for the hydrothermal-vapour condition, spaces free of cells were found on the strands (Figure 11(b)). This can be associated to the higher amount of pluronic F127 present in the hydrothermal-vapour scaffolds, as measured by TGA (Figure 4), since during the vapour treatment there is no chance for pluronic to be released prior to the cell culture, which could lead to a reduction of cell adhesion and compromise the cytocompatibility of the scaffold.[56] It can be concluded, therefore, that the immersion of the scaffold during hydrothermal treatment is a requisite not only to enhance the transformation of α-TCP to CDHA, with the consequent improvement of the mechanical properties, but also to facilitate the release of the binder and increase the cytocompatibility of the scaffold. Indeed, both biomimetic and hydrothermal-immersed treatments allowed cell colonisation. This is a promising result that supports the use of these scaffolds in cell-based bone tissue engineering therapies and the development of *in vitro* bone models.

4   Conclusion

In this study, we developed a hydrothermal method that allows a significant reduction in the consolidation time of DIW α-TCP scaffolds, without losing the biomimetic features. The hydrothermal treatment of DIW scaffolds immersed in water significantly accelerated the hydrolysis of α-TCP into CDHA, reducing the hardening time to 30 minutes. This offers the possibility to fabricate scaffolds on-demand in a very short lapse of time (e.g. few hours), including the time for patient imaging, scaffold architecture selection, DIW and consolidation. This can represent a paramount advantage, in particular to treat clinical emergencies such as car, labour or sport accidents, in a patient-specific way. The hydrothermal treatment of the scaffolds resulted in a change in microstructure and promoted the allotropic transformation of α-TCP into its β polymorph, which reduced the yield in CDHA formation and resulted in a slight decrease of strength

17

and reliability. Both the biomimetic and hydrothermal-immersed treatments resulted in scaffolds with compressive strengths similar to trabecular bone. Whereas a compressive strength of 5.51 MPa was obtained in HC scaffolds with 68.7% porosity with the biomimetic treatment, the hydrothermal-immersed treatment resulted in a compressive strength of 4.09 MPa for HC scaffolds with 72.6% porosity. The Weibull modulus was higher in the biomimetic treatment than in the hydrothermal-immersed treatment (8.79 vs. 5.62 respectively), indicating higher reliability. In addition, both treatments allowed the scaffold colonization by rMSC, suggesting that the two treatments are suitable to produce synthetic patient-specific bone grafts. However, due to the intrinsic brittleness of these materials, the use of such scaffolds in load bearing applications would require a further enhancement of their mechanical properties or the combination with additional mechanical fixation systems.

Acknowledgment

Disclosure

MPG and YM have an equity interest in Mimetis Biomaterials, S.L., a spin-off company of UPC that may potentially benefit from the research results displayed in the present work.

References

[1]   C.G. Finkemeier, Bone-grafting and bone-graft substitutes., J. Bone Joint Surg. Am. 84–A (2002) 454–64. http://www.ncbi.nlm.nih.gov/pubmed/11886919 (accessed December 19, 2017).

[2]   M. Bohner, Resorbable biomaterials as bone graft substitutes, Mater. Today. 13 (2010) 24–30. doi:10.1016/S1369-7021(10)70014-6.

[3]   B. Stevens, Y. Yang, A. Mohandas, B. Stucker, K.T. Nguyen, A review of materials, fabrication methods, and strategies used to enhance bone regeneration in engineered bone tissues, J. Biomed. Mater. Res. Part B Appl. Biomater. 85B (2008) 573–582. doi:10.1002/jbm.b.30962.

[4]   S. Bose, S. Vahabzadeh, A. Bandyopadhyay, Bone tissue engineering using 3D printing, Mater. Today. 16 (2013) 496–504. doi:10.1016/j.mattod.2013.11.017.

[5]   D. Tang, R.S. Tare, L.-Y. Yang, D.F. Williams, K.-L. Ou, R.O.C. Oreffo, Biofabrication of bone tissue: approaches, challenges and translation for bone regeneration, Biomaterials. 83 (2016) 363–382. doi:10.1016/j.biomaterials.2016.01.024.

[6]   A. Butscher, M. Bohner, S. Hofmann, L. Gauckler, R. Müller, Structural and material approaches to bone tissue engineering in powder-based three-dimensional printing, Acta Biomater. 7 (2011) 907–920. doi:10.1016/j.actbio.2010.09.039.

[7]   J.I. Cesarano, T.A. Baer, P. Calvert, Recent developments in freeform fabrication of dense ceramics from slurry deposition, Albuquerque, NM, and Livermore, CA (United States), TEXAS, 1997. doi:10.2172/554831.

[8]   J.E. Smay, J. Cesarano, J.A. Lewis, Colloidal Inks for Directed Assembly of 3-D Periodic Structures, Langmuir. 18 (2002) 5429–5437. doi:10.1021/la0257135.

[9]   S. Michna, W. Wu, J.A. Lewis, Concentrated hydroxyapatite inks for direct-write assembly of 3-D periodic scaffolds, Biomaterials. 26 (2005) 5632–5639. doi:10.1016/j.biomaterials.2005.02.040.

[10]   A. Kumar, A.R. Akkineni, B. Basu, M. Gelinsky, Three-dimensional plotted hydroxyapatite scaffolds with predefined architecture: comparison of stabilization by alginate cross-linking versus sintering, J. Biomater. Appl. 30 (2016) 1168–1181. doi:10.1177/0885328215617058.

[11]   P. Miranda, A. Pajares, E. Saiz, A.P. Tomsia, F. Guiberteau, Mechanical properties of calcium phosphate scaffolds fabricated by robocasting, J. Biomed. Mater. Res. Part A. 85A (2008) 218–227. doi:10.1002/jbm.a.31587.

[12]   P. Miranda, E. Saiz, K. Gryn, A.P. Tomsia, Sintering and robocasting of β-tricalcium phosphate scaffolds for orthopaedic applications, Acta Biomater. 2 (2006) 457–466. doi:10.1016/j.actbio.2006.02.004.

[13]   Y. Zhang, L. Xia, D. Zhai, M. Shi, Y. Luo, C. Feng, B. Fang, J. Yin, J. Chang, C. Wu, Mesoporous bioactive glass nanolayer-functionalized 3D-printed scaffolds for accelerating osteogenesis and angiogenesis, Nanoscale. 7 (2015) 19207–19221. doi:10.1039/C5NR05421D.

[14]   M. Houmard, Q. Fu, M. Genet, E. Saiz, A.P. Tomsia, On the structural, mechanical, and biodegradation properties of HA/β-TCP robocast scaffolds, J. Biomed. Mater. Res. Part B Appl. Biomater. 101 (2013) 1233–1242. doi:10.1002/jbm.b.32935.

[15]   C. Mangano, B. Barboni, L. Valbonetti, P. Berardinelli, A. Martelli, A. Muttini, R. Bedini, S. Tetè, A. Piattelli, M. Mattioli, In Vivo Behavior of a Custom-Made 3D Synthetic Bone Substitute in Sinus

19

Augmentation Procedures in Sheep, J. Oral Implantol. 41 (2015) 240–250. doi:10.1563/AAID-JOI-D-13-00053.

[16]   J. Franco, P. Hunger, M.E. Launey, A.P. Tomsia, E. Saiz, Direct write assembly of calcium phosphate scaffolds using a water-based hydrogel, Acta Biomater. 6 (2010) 218–228. doi:10.1016/j.actbio.2009.06.031.

[17]   S. Ishack, A. Mediero, T. Wilder, J.L. Ricci, B.N. Cronstein, Bone regeneration in critical bone defects using three-dimensionally printed β-tricalcium phosphate/hydroxyapatite scaffolds is enhanced by coating scaffolds with either dipyridamole or BMP-2, J. Biomed. Mater. Res. Part B Appl. Biomater. 105 (2017) 366–375. doi:10.1002/jbm.b.33561.

[18]   Q. Fu, E. Saiz, A.P. Tomsia, Bioinspired Strong and Highly Porous Glass Scaffolds, Adv. Funct. Mater. 21 (2011) 1058–1063. doi:10.1002/adfm.201002030.

[19]   X. Liu, M.N. Rahaman, G.E. Hilmas, B.S. Bal, Mechanical properties of bioactive glass (13-93) scaffolds fabricated by robotic deposition for structural bone repair, Acta Biomater. 9 (2013) 7025–7034. doi:10.1016/j.actbio.2013.02.026.

[20]   Y. Luo, A. Lode, C. Wu, M. Gelinsky, 3D Plotting of Bioceramic Scaffolds under Physiological Conditions for Bone Tissue Engineering, in: Adv. Bioact. Inorg. Mater. Bone Regen. Drug Deliv., CRC Press, 2013: pp. 83–116. doi:10.1201/b13926-5.

[21]   C. Wu, Y. Luo, G. Cuniberti, Y. Xiao, M. Gelinsky, Three-dimensional printing of hierarchical and tough mesoporous bioactive glass scaffolds with a controllable pore architecture, excellent mechanical strength and mineralization ability, Acta Biomater. 7 (2011) 2644–2650. doi:10.1016/j.actbio.2011.03.009.

[22]   A. Motealleh, S. Eqtesadi, F.H. Perera, A. Pajares, F. Guiberteau, P. Miranda, Understanding the role of dip-coating process parameters in the mechanical performance of polymer-coated bioglass robocast scaffolds, J. Mech. Behav. Biomed. Mater. 64 (2016) 253–261. doi:10.1016/j.jmbbm.2016.08.004.

[23]   H. Yun, S. Kim, Y. Hyeon, Design and preparation of bioactive glasses with hierarchical pore networks, Chem. Commun. (2007) 2139. doi:10.1039/b702103h.

[24]   S. Eqtesadi, A. Motealleh, P. Miranda, A. Lemos, A. Rebelo, J.M.F. Ferreira, A simple recipe for direct writing complex 45S5 Bioglass® 3D scaffolds, Mater. Lett. 93 (2013) 68–71. doi:10.1016/j.matlet.2012.11.043.

[25]   A. Vallés Lluch, A. Campillo Fernández, G. Gallego Ferrer, M. Monleón Pradas, Bioactive scaffolds mimicking natural dentin structure, J. Biomed. Mater. Res. Part B Appl. Biomater. 90B (2008) 182–194. doi:10.1002/jbm.b.31272.

[26]   D.J. Hoelzle, A.G. Alleyne, A.J. Wagoner Johnson, Micro-robotic deposition guidelines by a design of experiments approach to maximize fabrication reliability for the bone scaffold application, Acta Biomater. 4 (2008) 897–912. doi:10.1016/j.actbio.2008.02.018.

[27]   C. Wu, W. Fan, Y. Zhou, Y. Luo, M. Gelinsky, J. Chang, Y. Xiao, 3D-printing of highly uniform CaSiO3 ceramic scaffolds: preparation, characterization and in vivo osteogenesis, J. Mater. Chem. 22 (2012) 12288. doi:10.1039/c2jm30566f.

[28]   M.M. Farag, H.S. Yun, Effect of gelatin addition on fabrication of magnesium phosphate-based scaffolds prepared by additive manufacturing system, Mater. Lett. 132 (2014) 111–115. doi:10.1016/j.matlet.2014.06.055.

[29]   Y. Maazouz, E.B. Montufar, J. Guillem-Marti, I. Fleps, C. Öhman, C. Persson, M.P. Ginebra, Robocasting of biomimetic hydroxyapatite scaffolds using self-setting inks, J. Mater. Chem. B. 2 (2014) 5378–5386. doi:10.1039/C4TB00438H.

[30]   A. Lode, K. Meissner, Y. Luo, F. Sonntag, S. Glorius, B. Nies, C. Vater, F. Despang, T. Hanke, M. Gelinsky, Fabrication of porous scaffolds by three-dimensional plotting of a pasty calcium phosphate bone cement under mild conditions, J. Tissue Eng. Regen. Med. 8 (2014) 682–693. doi:10.1002/term.1563.

[31]   W.J. Kim, H. Yun, G.H. Kim, An innovative cell-laden α-TCP/collagen scaffold fabricated using a two-step printing process for potential application in regenerating hard tissues, Sci. Rep. 7 (2017) 3181. doi:10.1038/s41598-017-03455-9.

[32]   N. Raja, H. Yun, A simultaneous 3D printing process for the fabrication of bioceramic and cell-laden hydrogel core/shell scaffolds with potential application in bone tissue regeneration, J. Mater. Chem. B. 4 (2016) 4707–4716. doi:10.1039/C6TB00849F.

[33]   Y. Luo, A. Lode, F. Sonntag, B. Nies, M. Gelinsky, Well-ordered biphasic calcium phosphate–alginate scaffolds fabricated by multi-channel 3D plotting under mild conditions, J. Mater. Chem. B. 1 (2013) 4088. doi:10.1039/c3tb20511h.

[34]   A.R. Akkineni, Y. Luo, M. Schumacher, B. Nies, A. Lode, M. Gelinsky, 3D plotting of growth factor loaded calcium phosphate cement scaffolds, Acta Biomater. 27 (2015) 264–274. doi:10.1016/j.actbio.2015.08.036.

[35]   Y. Maazouz, E.B. Montufar, J. Malbert, M. Espanol, M.-P.P. Ginebra, Self-hardening and thermoresponsive alpha tricalcium phosphate/pluronic pastes, Acta Biomater. 49 (2017) 563–574. doi:10.1016/j.actbio.2016.11.043.

[36]   E.B. Montufar, Y. Maazouz, M.P. Ginebra, Relevance of the setting reaction to the injectability of tricalcium phosphate pastes, Acta Biomater. 9 (2013) 6188–6198. doi:10.1016/j.actbio.2012.11.028.

[37]   D. Pastorino, C. Canal, M.-P. Ginebra, Multiple characterization study on porosity and pore structure of calcium phosphate cements, Acta Biomater. 28 (2015) 205–214. doi:10.1016/j.actbio.2015.09.017.

[38]   M.P. Ginebra, E. Fernández, E.A.P. De Maeyer, R.M.H. Verbeeck, M.G. Boltong, J. Ginebra, F.C.M. Driessens, J.A. Planell, Setting Reaction and Hardening of an Apatitic Calcium Phosphate Cement, J. Dent. Res. 76 (1997) 905–912. doi:10.1177/00220345970760041201.

[39]   M.-P. Ginebra, E. Fernández, F.C.M. Driessens, J.A. Planell, Modeling of the Hydrolysis of α-Tricalcium Phosphate, J. Am. Ceram. Soc. 82 (2004) 2808–2812. doi:10.1111/j.1151-2916.1999.tb02160.x.

[40]   M.P. Ginebra, E. Fernández, F.C.M. Driessens, M.G. Boltong, J. Muntasell, J. Font, J.A. Planell, The effects of temperature on the behaviour of an apatitic calcium phosphate cement, J. Mater. Sci. Mater. Med. 6 (1995) 857–860. doi:10.1007/BF00134332.

[41]   C. Durucan, P.W. Brown, Kinetic Model for α-Tricalcium Phosphate Hydrolysis, J. Am. Ceram. Soc. 85 (2002) 2013–2018. doi:10.1111/j.1151-2916.2002.tb00397.x.

[42]   C. Rey, C. Combes, C. Drouet, D. Grossin, G. Bertrand, J. Soulié, Bioactive Calcium Phosphate Compounds: Physical Chemistry, in: Compr. Biomater. II, Elsevier, 2017: pp. 244–290. doi:10.1016/B978-0-12-803581-8.10171-7.

[43]   R.G. Carrodeguas, S. De Aza, α-Tricalcium phosphate: Synthesis, properties and biomedical

21

applications, Acta Biomater. 7 (2011) 3536–3546. doi:10.1016/j.actbio.2011.06.019.

[44] L. Galea, D. Alexeev, M. Bohner, N. Doebelin, A.R. Studart, C.G. Aneziris, T. Graule, Textured and hierarchically structured calcium phosphate ceramic blocks through hydrothermal treatment, Biomaterials. 67 (2015) 93–103. doi:10.1016/j.biomaterials.2015.07.026.

[45] T.I. Ivanova, O.V. Frank-Kamenetskaya, A.B. Kol'tsov, V.L. Ugolkov, Crystal Structure of Calcium-Deficient Carbonated Hydroxyapatite. Thermal Decomposition, J. Solid State Chem. 160 (2001) 340–349. doi:10.1006/jssc.2000.9238.

[46] J.C. Elliott, General Chemistry of the Calcium Orthophosphates, in: Stud. Org. Chem., 1994: pp. 1–62. doi:10.1016/B978-0-444-81582-8.50006-7.

[47] V.M. Bhatnagar, Infrared spectrum of strontium hydroxyapatite, Experientia. 23 (1967) 697–699. doi:10.1007/BF02154118.

[48] R.M. Wilson, J.C. Elliott, S.E.P. Dowker, L.M. Rodriguez-Lorenzo, Rietveld refinements and spectroscopic studies of the structure of Ca-deficient apatite, Biomaterials. 26 (2005) 1317–1327. doi:10.1016/j.biomaterials.2004.04.038.

[49] M. Mir, F.L. Leite, P.S. de P. Herrmann Junior, F.L. Pissetti, A.M. Rossi, E.L. Moreira, Y.P. Mascarenhas, XRD, AFM, IR and TGA study of nanostructured hydroxyapatite, Mater. Res. 15 (2012) 622–627. doi:10.1590/S1516-14392012005000069.

[50] C. Guo, H.-Z. Liu, J.-Y. Chen, A Fourier transform infrared study of the phase transition in aqueous solutions of Ethylene oxide-propylene oxide triblock copolymer, Colloid Polym. Sci. 277 (1999) 376–381. doi:10.1007/s003960050395.

[51] M. Espanol, R.A. Perez, E.B. Montufar, C. Marichal, A. Sacco, M.P. Ginebra, Intrinsic porosity of calcium phosphate cements and its significance for drug delivery and tissue engineering applications, Acta Biomater. 5 (2009) 2752–2762. doi:10.1016/j.actbio.2009.03.011.

[52] K. Ioku, G. Kawachi, S. Sasaki, H. Fujimori, S. Goto, Hydrothermal preparation of tailored hydroxyapatite, J. Mater. Sci. 41 (2006) 1341–1344. doi:10.1007/s10853-006-7338-5.

[53] S. Gallinetti, C. Canal, M.-P. Ginebra, Development and Characterization of Biphasic Hydroxyapatite/β-TCP Cements, J. Am. Ceram. Soc. 97 (2014) 1065–1073. doi:10.1111/jace.12861.

[54] D.W. Hutmacher, J.T. Schantz, C.X.F. Lam, K.C. Tan, T.C. Lim, State of the art and future directions of scaffold-based bone engineering from a biomaterials perspective., J. Tissue Eng. Regen. Med. 1 (n.d.) 245–60. doi:10.1002/term.24.

[55] P. Miranda, A. Pajares, E. Saiz, A.P. Tomsia, F. Guiberteau, Fracture modes under uniaxial compression in hydroxyapatite scaffolds fabricated by robocasting, J. Biomed. Mater. Res. Part A. 83A (2007) 646–655. doi:10.1002/jbm.a.31272.

[56] T. Tharmalingam, H. Ghebeh, T. Wuerz, M. Butler, Pluronic Enhances the Robustness and Reduces the Cell Attachment of Mammalian Cells, Mol. Biotechnol. 39 (2008) 167–177. doi:10.1007/s12033-008-9045-8.

Figure Legends

Figure 1. Different patterns employed for the scaffolds.

Figure 2. Schematic representation of the different post-printing treatments tested in this study: (a) Biomimetic treatment, (b) Hydrothermal-immersed treatment, and (c) Hydrothermal-vapour treatment.

Figure 3. Phase transformation kinetics determined by XRD analysis for the different hardening conditions.

Figure 4. (a) Thermogravimetric mass loss of the samples subjected to the different post-printing treatments, where the continuous and the dashed lines correspond to the studied scaffolds and their pluronic-free counterparts respectively. The mass loss for the pure pluronic F127 is represented in the inset; (b) amount of pluronic F127 calculated from the TGA data, where the dashed line indicates the binder nominal concentration in the ink.

Figure 5. KBr-Fourier Transformed Infrared spectroscopy diagrams of the scaffolds subjected to the different post-printing treatments.

Figure 6. Representative Field Emission-Scanning Electron Microscopy images of the microstructures obtained at two different magnifications after the different post-printing treatments: (a) Biomimetic, 7 days; (b) Hydrothermal-immersed, 30 minutes; and (c) Hydrothermal-vapour, 100 minutes.

Figure 7. Pore entrance size distribution obtained by mercury intrusion porosimetry (MIP) for HC pattern scaffolds subjected to the different post-printing treatments.

Figure 8. (a) Porosity and (b) compressive strength and Weibull modulus of the scaffolds printed with HC pattern and subjected to the different post-printing treatments. (c) Porosity and (d) compressive strength and Weibull modulus of the scaffolds set by the biomimetic treatment printed with different patterns. Statistically significant differences between treatments (b) and between patterns (d) are marked with different letters.

Figure 9. Virtual reconstructions from μ-CT data of scaffolds printed with different patterns. Top: vertical view from the printing plane; middle: unit cells representing the solid part of the cell (light grey) and rendered porosity (red); bottom: centro-lateral view showing the pillars that transfer the mechanical load during compression strength test, blue arrows show the continuity of the pillars in the direction of loading.

Figure 10. Top: Overlapped axial view of the repetition units for each pattern. Bottom: Regions of the cross sections that are common in all the layers. This pattern renders immediate comprehension of the scaffold pillars morphology. The image is a result of a Boolean AND operation with the binarised images of the cross sections constituting the repetition unit.

Figure 11. Results of the cell culture study: (a) Number of rMSC determined by LDH assay after 3 and 7 days of 3D static cell culture on O scaffolds subjected to the different post-printing treatments where different letters indicate statistically significant differences; and (b-d) confocal microscope images of cells attached to these scaffolds after 7 days of 3D static cell culture. Actin cytoskeleton is shown in red and nuclei in blue.
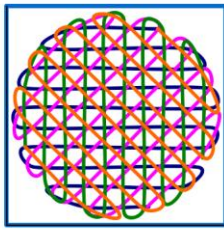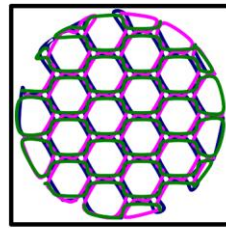
Orthogonal
(O)

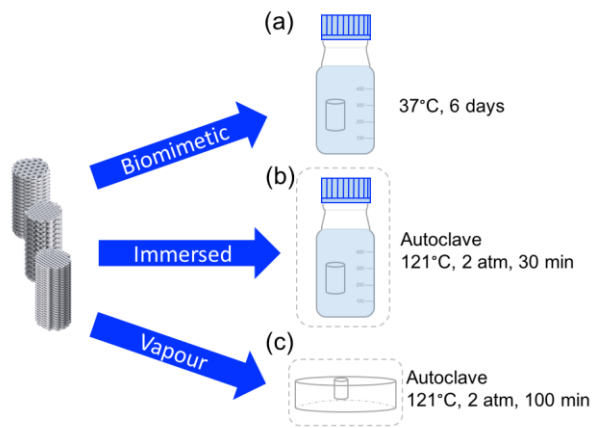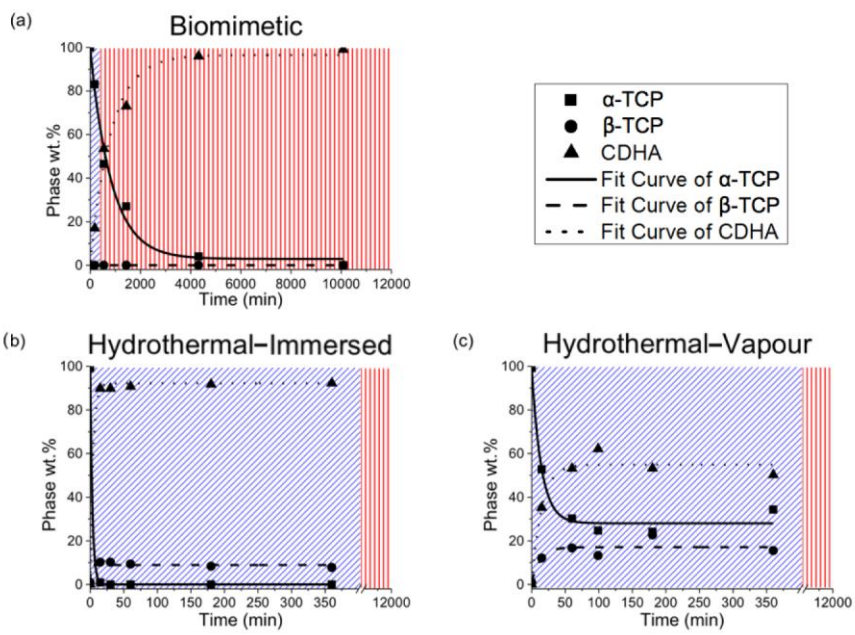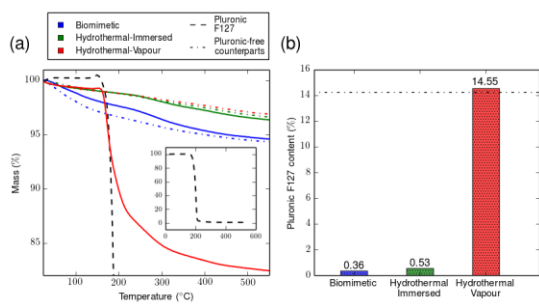Orthogonal rotated
(OR)

Honeycomb
(HC)
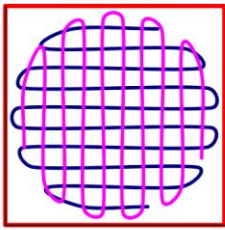
AB

ABCD

ABC

(a) 37°C, 6 days

(b) Autoclave
121°C, 2 atm, 30 min

(c) Autoclave
121°C, 2 atm, 100 min

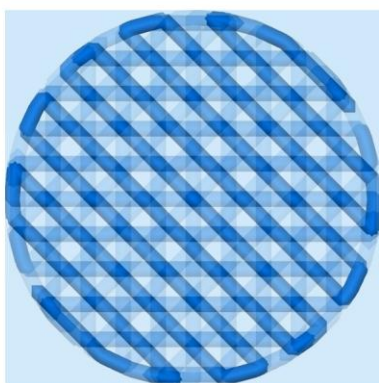Biomimetic

Immersed

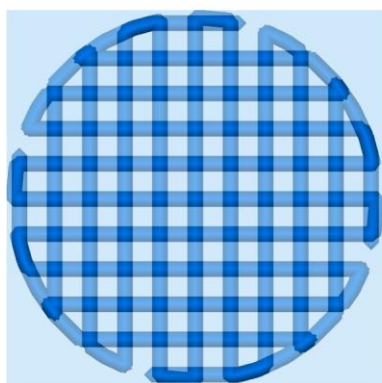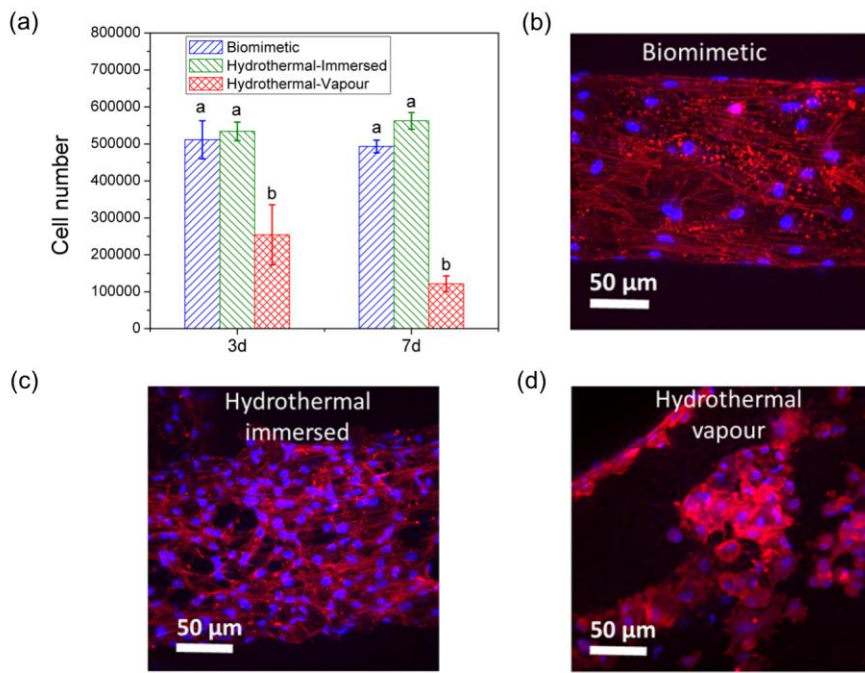Vapour

(a)

(b)

(c)

(d)

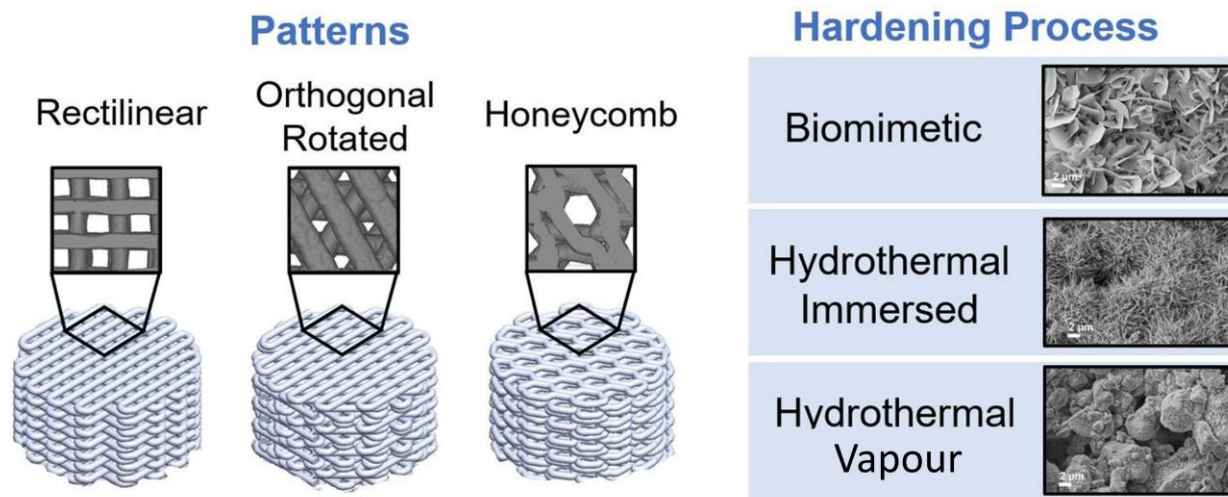R OR HC

(a)

(b)

(c)

(d)
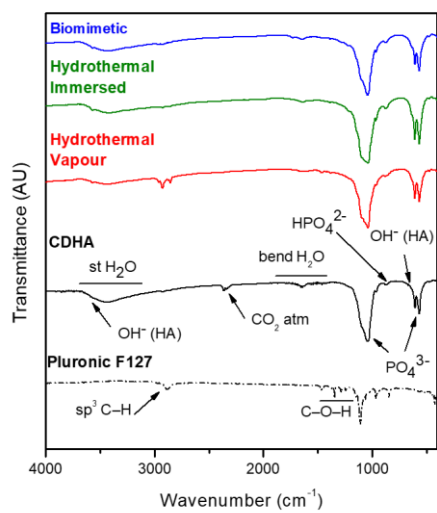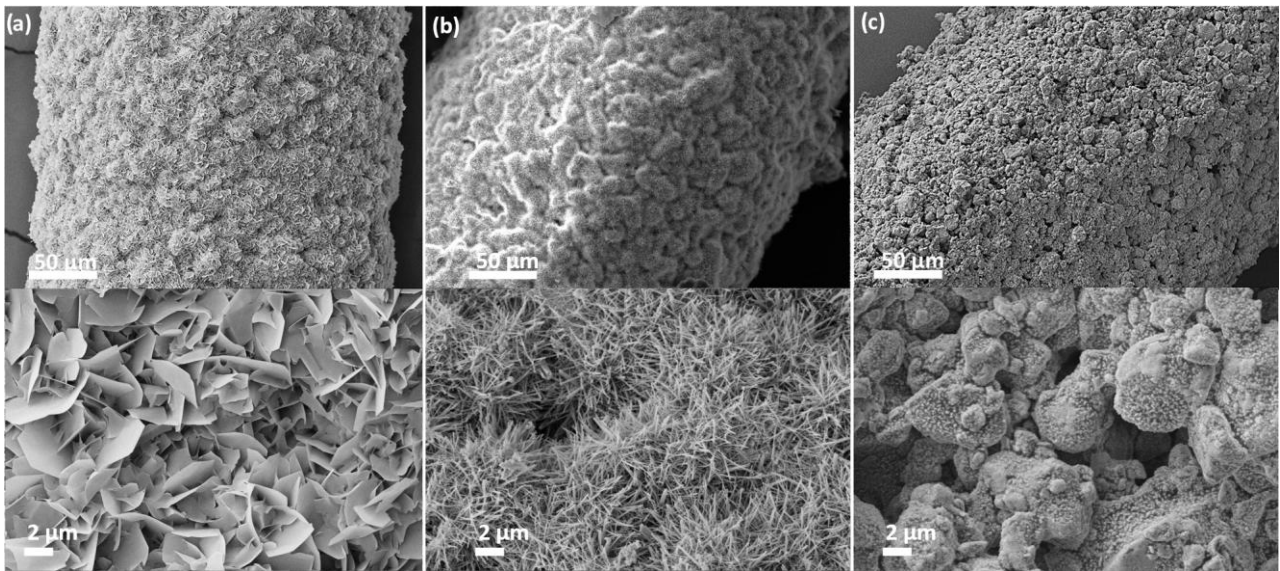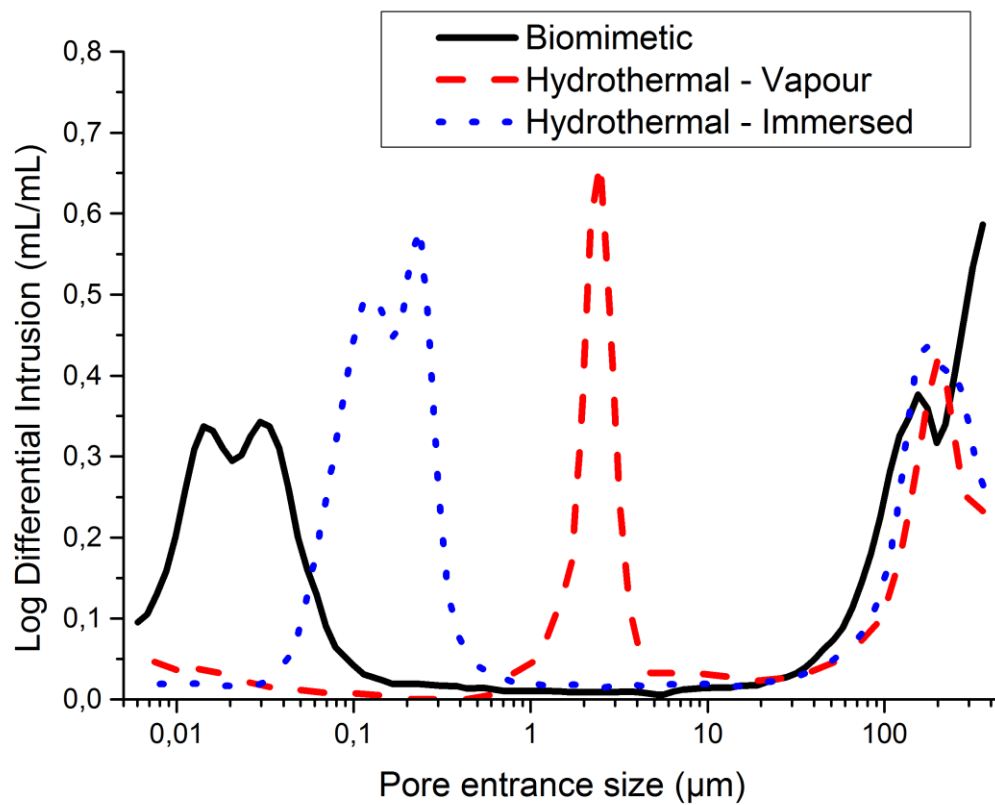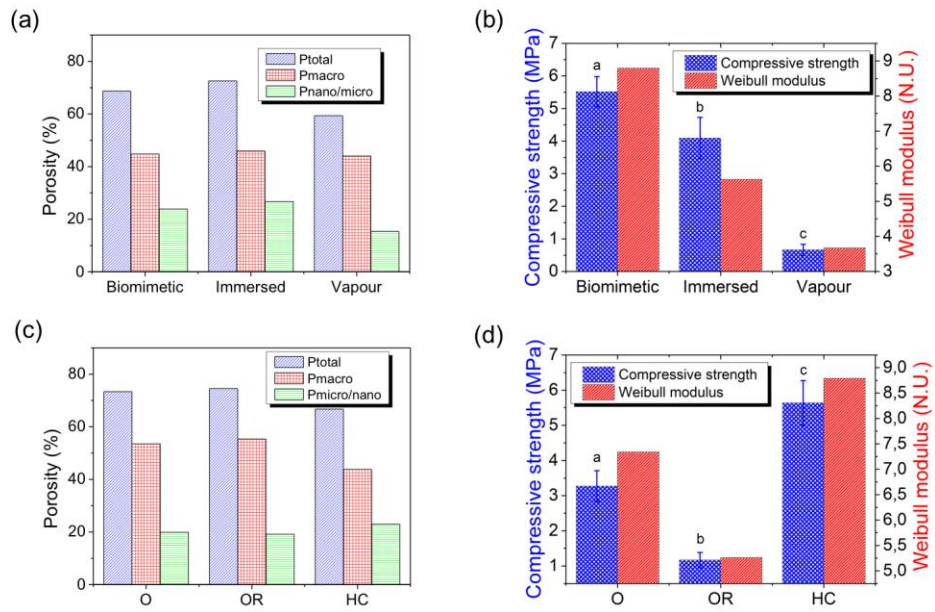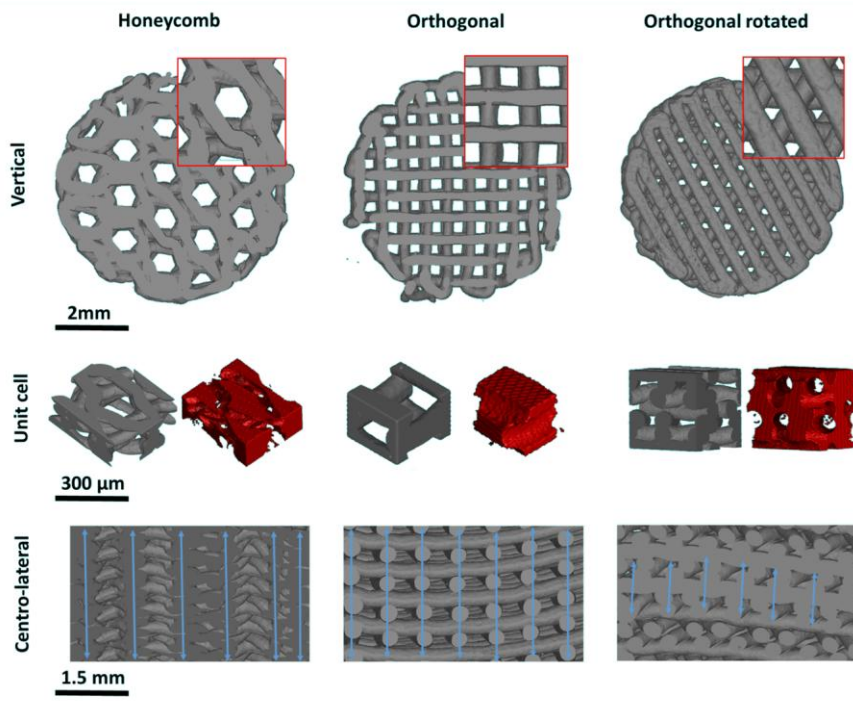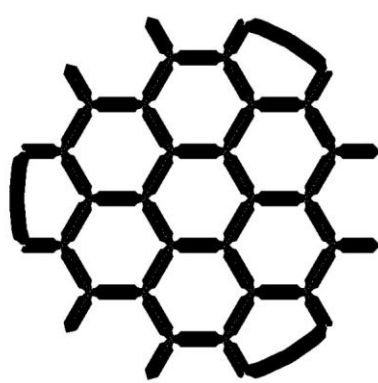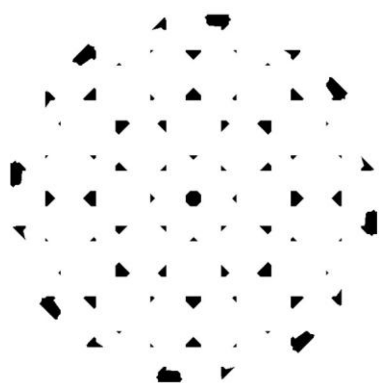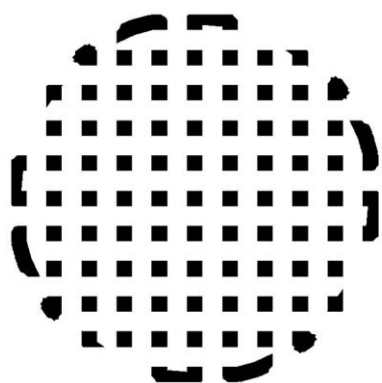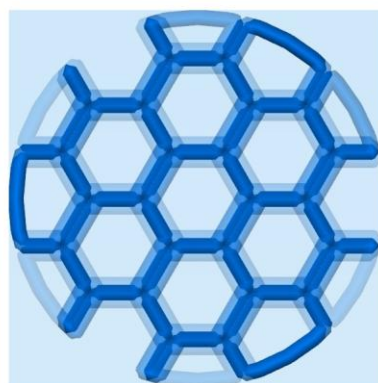
Statement of significance

3D plotting has opened up new perspectives in the bone regeneration field allowing the customization of synthetic bone grafts able to fit patient-specific bone defects. Moreover, this technique allows the control of the scaffolds' architecture and porosity. The present work introduces a new method to harden biomimetic hydroxyapatite 3D-plotted scaffolds which avoids high-temperature sintering. It has two main advantages: i) it is fast and simple, reducing the whole fabrication process from the several days required for the biomimetic processing to few hours; and ii) it retains the nanostructured character of biomimetic hydroxyapatite and allows controlling the porosity from the nano- to the macroscale. Moreover, the good *in vitro* cytocompatibility results support its suitability for cell-based bone regeneration therapies.

Graphical abstrct